Mesoscale Energy Spectra of Moist Baroclinic Waves

MICHAEL L. WAITE

University of Waterloo, Waterloo, Ontario, Canada

CHRIS SNYDER

National Center for Atmospheric Research, Boulder, Colorado*

(Manuscript received 28 December 2011, in final form 9 November 2012)

ABSTRACT

The role of moist processes in the development of the mesoscale kinetic energy spectrum is investigated with numerical simulations of idealized moist baroclinic waves. Dry baroclinic waves yield upper-tropospheric kinetic energy spectra that resemble a -3 power law. Decomposition into horizontally rotational and divergent kinetic energy shows that the divergent energy has a much shallower spectrum, but its amplitude is too small to yield a characteristic kink in the total spectrum, which is dominated by the rotational part. The inclusion of moist processes energizes the mesoscale. In the upper troposphere, the effect is mainly in the divergent part of the kinetic energy; the spectral slope remains shallow (around $-5/3$) as in the dry case, but the amplitude increases with increasing humidity. The divergence field in physical space is consistent with inertia–gravity waves being generated in regions of latent heating and propagating throughout the baroclinic wave. Buoyancy flux spectra are used to diagnose the scale at which moist forcing—via buoyant production from latent heating—injects kinetic energy. There is significant input of kinetic energy in the mesoscale, with a peak at scales of around 800 km and a plateau at smaller scales. If the latent heating is artificially set to zero at some time, the enhanced divergent kinetic energy decays over several days toward the level obtained in the dry simulation. The effect of moist forcing of mesoscale kinetic energy presents a challenge for theories of the mesoscale spectrum based on the idealization of a turbulent inertial subrange.

1. Introduction

The mesoscale plays an important role in the atmospheric energy budget by linking the large, energy-containing planetary and synoptic scales with the microscale where turbulent dissipation occurs. Observations of the atmospheric kinetic energy (KE) spectrum show a distinct spectral transition in the mesoscale: whereas the synoptic scales exhibit an approximately -3 power law in agreement with quasigeostrophic turbulence theory (Charney 1971), the mesoscale has a much shallower slope that has been identified as $-5/3$ (e.g., Gage 1979; Nastrom and Gage 1985; Cho et al. 1999a). Despite early questions about the direction of energy flow through the mesoscale (e.g., Dewan 1979; Gage 1979; VanZandt 1982; Lilly 1983), observational evidence points to a downscale transfer of kinetic energy from the synoptic scale toward the microscale (Lindborg and Cho 2001). Over the last decade, the mesoscale energy spectrum has been reproduced in a variety of numerical simulations of the atmosphere, using both global (Koshyk and Hamilton 2001; Takahashi et al. 2006; Hamilton et al. 2008) and regional (Skamarock 2004; Skamarock and Klemp 2008) models. The transition from a -3 power law to a shallower spectrum has also been reproduced in more idealized models, including rotating–stratified Boussinesq (Kitamura and Matsuda 2010; Bartello 2010) and surface quasigeostrophic (Tulloch and Smith 2009) models. However, significant questions remain about the dynamics of energy transfer through the mesoscale.

Since Gage (1979) recognized that the mesoscale spectral slope is close to $-5/3$—the theoretical slope for the direct energy cascade in isotropic three-dimensional

* The National Center for Atmospheric Research is sponsored by the National Science Foundation.

Corresponding author address: Michael L. Waite, Department of Applied Mathematics, University of Waterloo, 200 University Ave. W., Waterloo, ON N2L 3G1, Canada.
E-mail: mwaite@uwaterloo.ca

DOI: 10.1175/JAS-D-11-0347.1

turbulence (Kolmogorov 1941) and the inverse cascade in two dimensions (Kraichnan 1967)—there have been a number of attempts to identify a turbulent cascade phenomenology for the mesoscale. Some early theories, which posited an inverse energy cascade in analogy with two-dimensional turbulence (Gage 1979; Lilly 1983), have been ruled out by Lindborg and Cho (2001). However, a variety of downscale cascade mechanisms have been identified, including nonlinearly interacting inertia–gravity waves (IGWs) (Dewan 1979; VanZandt 1982), double cascades in quasigeostrophic turbulence (Tung and Orlando 2003; Gkioulekas and Tung 2005a,b), anisotropic turbulence with strong stable density stratification (Lindborg 2006), and surface quasigeostrophic turbulence near the tropopause (Tulloch and Smith 2009).

A common approach for investigating the consistency between numerical simulations, observations, and theory is to decompose the kinetic energy into horizontally rotational and divergent contributions (RKE and DKE, respectively). This decomposition gives an approximate separation into balanced (rotational) and inertia–gravity wave (divergent) contributions. This separation is fairly crude, as IGWs can have nonzero RKE $\leq$ DKE (with equality for pure inertia waves) and balanced flows have small but nonzero divergence. Nevertheless it is a useful decomposition that is straightforward to apply to model output. Hamilton et al. (2008) found that the RKE spectrum transitions from -3 to something shallower below scales of around 500 km; their mesoscale spectrum is dominated by RKE, with DKE around 3 times smaller. By contrast, Skamarock and Klemp (2008) found equipartition of rotational and divergent energy in the mesoscale, with both spectra following a $-5/3$ slope below scales of around 400 km. Observational studies have also shown a slight dominance of RKE in the mesoscale, at least in midlatitudes (Cho et al. 1999b; Lindborg 2007). In particular, Lindborg (2007) reanalyzed structure functions from aircraft data and found a broad spectral transition at scales of around 100 km, below which DKE and RKE followed a $-5/3$ slope with a ratio of around $2/3$. Lindborg concluded that IGWs alone cannot account for the shape of the spectrum below this transition, given the relative amplitude of the RKE.

Implicit in all of these proposed theories for the mesoscale spectrum is the assumption that it can be idealized as a turbulent inertial subrange—that is, that kinetic energy is transferred to successively smaller and smaller scales in a conservative manner (e.g., Davidson 2004). In particular, these cascade theories require that the mesoscale not be a significant source or sink of KE. However, many physical phenomena in mesoscale meteorology have the potential to add or remove kinetic energy. An important example is latent heating, by which moisture can generate buoyancy perturbations that may inject kinetic energy across a range of scales, including the mesoscale. Other processes that may modify mesoscale energetics include wave generation over topography, boundary layer drag, and radiative cooling. Depending on their strength, these processes may impact the mesoscale KE budget and the resulting spectrum, but they are largely neglected by the cascade theories listed above. In the case of moisture, numerical simulations suggest that it can have a significant influence on the energy and spectral characteristics of the mesoscale. Hamilton et al. (2008) compared mesoscale spectra in global simulations with and without moisture and topography. The mesoscale kinetic energy spectrum in the dry simulations had a smaller amplitude and steeper slope than corresponding moist-physics simulations. Topography, by contrast, had a much smaller effect on the mesoscale spectrum.

In this work, we present numerical experiments that investigate the role of moist processes in the formation of a mesoscale spectrum in an idealized baroclinic wave. Baroclinic life cycle experiments are a commonly used prototype for midlatitude dynamics, as they naturally develop a variety of mesoscale structures that are present in the real atmosphere and more comprehensive simulations, including IGWs, fronts, and jets (e.g., Snyder et al. 1991; O'Sullivan and Dunkerton 1995; Plougonven and Snyder 2007, hereafter PS; Waite and Snyder 2009, hereafter WS). In WS, we analyzed the mesoscale spectrum in a high-resolution dry baroclinic life cycle simulation. The initial jet was quite strong, and the resulting baroclinic wave saturated at a realistic amplitude and Rossby number. Nevertheless, the resulting mesoscale kinetic energy spectrum had a much lower amplitude, and was steeper—closer to -3 than $-5/3$—than the observed spectrum. Interestingly, we found that the horizontally divergent part of the kinetic energy spectrum had a spectral slope that was very close to $-5/3$, consistent with a downscale cascade of inertia–gravity wave energy. However, the amplitude of the divergent spectrum was much lower than that of the rotational kinetic energy, so it did not lead to a transition to a shallower spectrum of total kinetic energy. A natural question raised by this work was whether missing moist physics might amplify the mesoscale spectrum in baroclinic wave simulations; we address this question here.

Including moisture and the attendant latent heat release in baroclinic wave simulations typically accelerates their development and causes minor changes to the mesoscale structures that appear. Simplified, theoretical studies indicate that latent heating provides an additional mechanism for growth at synoptic scales (e.g., Snyder and Lindzen 1991) and will accelerate frontogenesis (Thorpe and Emanuel 1985). Both effects are

apparent in the life cycle experiments of Whitaker and Davis (1994) that include a parameterization of latent heating in ascending air; they find more rapid growth of the baroclinic wave and significant enhancement of the warm front northwest of the surface cyclone.

Here we extend WS to consider the effects of moisture on the mesoscale spectrum. Based on the findings of Hamilton et al. (2008), we expect latent heating from convection and stable ascent to energize the mesoscale by buoyant production of kinetic energy. We start by verifying this relationship in the idealized framework of a baroclinic wave and quantifying the dependence of the spectrum on the degree of humidity. Our focus is on the upper troposphere, where heating and buoyant production is expected to occur, rather than the lower stratosphere, which is dominated by vertical propagation (e.g., Koshyk and Hamilton 2001; WS). In addition, we diagnose the scales at which latent heating adds kinetic energy to the atmosphere. Two possible scenarios are

1) large-scale forcing: kinetic energy is injected mainly at large scales, thereby enhancing the downscale cascade of kinetic energy and energizing the mesoscale, and
2) direct forcing of the mesoscale: kinetic energy is injected at mesoscale length scales, which directly energizes the mesoscale.

Both scenarios, or a combination of the two, are possible. However, these hypotheses have very different implications for the cascade theories of the mesoscale. Scenario 1 is consistent with the cascade theories since it implies enhancement of the large scales by moisture; the mesoscale is therefore affected only by a strengthening of the cascade (via IGWs, stratified turbulence, etc.) of energy through it. However, scenario 2 would require a reconsideration of the cascade theory, as it implies that direct forcing of the mesoscale is important.

The remainder of the manuscript is organized as follows. The initial conditions and simulation setup is outlined in section 2, and an overview of the simulations is given in section 3. Kinetic energy spectra are presented in section 4, where both horizontal wavenumber spectra, which facilitate the decomposition into rotational and divergent contributions, and zonal wavenumber spectra, which facilitate comparison with observations, are discussed. An analysis of the buoyancy flux, through which latent heating may force mesoscale kinetic energy, is given in section 5. Sensitivity to cumulus and microphysics parameterizations and numerical resolution is considered in section 6 and conclusions are given in section 7.

2. Approach

We employ the Advanced Research dynamical core of the Weather Research and Forecasting (WRF) model (Skamarock et al. 2008), which solves the equations of motion for a compressible, nonhydrostatic atmosphere. The model configuration is a midlatitude f plane in a rectangular channel with periodic boundary conditions in the zonal direction x and rigid boundaries (symmetric boundary conditions) in the meridional direction y. The horizontal extent of the domain is $L_x \times L_y = 4000$ km $\times$ 10 000 km, with a grid spacing of $\Delta x = \Delta y = 25$ km. Sensitivity to the horizontal resolution is discussed in section 4. The vertical grid comprises 180 layers over a depth of 30 km with an approximately uniform level spacing of $\Delta z \approx 110$ m in the troposphere, coarsening to 700 m near the upper boundary. This is higher vertical resolution than has been employed in most other computational studies of the mesoscale spectrum; for example, Skamarock (2004) and Skamarock and Klemp (2008) used $\Delta z \approx 250$ m near the surface, coarsening to around 1 km in the lower stratosphere (for details, see Done et al. 2004), while Hamilton et al. (2008) had a much coarser vertical grid with $\Delta z \approx 1.5$ km in the upper troposphere.

Simulations are initialized at $t = 0$ with a baroclinically unstable zonal jet perturbed with the fastest growing normal mode. A dry jet is constructed following previous studies on baroclinic waves in channel geometry (Rotunno et al. 1994; PS; WS; Davis 2010): the initial potential vorticity (PV) is assumed to be approximately uniform in the troposphere and stratosphere, with a smooth transition through a tropopause of prescribed form. Our parameter values follow the cyclonic case of PS, but are adjusted for a deeper domain and to keep the surface temperature reasonable. The PV is then inverted for the balanced dry dynamical fields. This inversion yields a strong jet centered at a height of ~9 km, with a maximum velocity of 56 m s^{-1} (Fig. 1). The most unstable mode is computed with the iterative breeding procedure of PS and is scaled to give a maximum potential temperature perturbation of 2 K [following Davis (2010), and larger than the perturbation of WS]. WS showed that this jet yields a synoptic-scale flow with a realistic amplitude and Rossby number.

Moisture is introduced in the initialization process after the PV inversion stage. The water vapor mixing ratio is set to yield a uniform relative humidity of 30% or 50%, referred to as RH30 and RH50, respectively. To compensate for the buoyancy of the vapor field, which would otherwise perturb the initial jet out of geostrophic balance, the temperature is adjusted down slightly so that the virtual temperature fields of the moist jets are

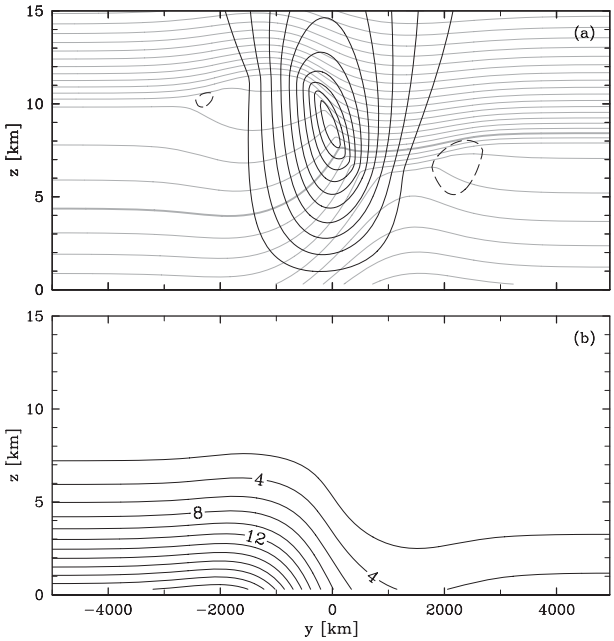

FIG. 1. Vertical slice through the initial moist (RH50) jet showing (a) zonal velocity (black contours, interval 5 m s^{-1}) and potential temperature (gray contours, interval 5 K) and (b) vapor mixing ratio (contour interval 2 g kg^{-1}). The 330-K potential temperature contour is thick, the zero velocity contour is omitted, and negative velocity contours are dashed. For clarity, only the lower 15 km of the domain is shown.

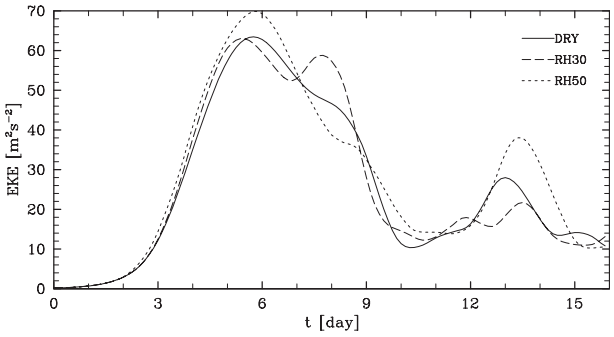

FIG. 2. Time series of eddy kinetic energy per unit mass, computed using the velocity fluctuations from the zonal average flow. The figure shows the mass-weighted average over the entire domain.

equal to that of the dry jet. As a result, the dry and moist simulations have identical initial conditions as far as the adiabatic dynamics are concerned. Because of this slight change to the temperature field, the actual relative humidity of the initial jet is nonuniform and larger than the prescribed values: the maximum humidity is around 40% for RH30 and 70% for RH50. The moist jets are perturbed with the dry normal mode.

After initialization, the simulations are run for 16 days. Moist processes are parameterized with the Janjić (1994) version of the Betts–Miller convection scheme (Betts and Miller 1986) and Kessler (1969) microphysics. Sensitivity to these parameterizations is considered in section 6. As our interest is on the effect of moisture on the mesoscale energy cascade, we use as few additional physical parameterizations as possible: in particular, no radiation scheme, surface fluxes, or boundary layer model are employed. Following Skamarock (2004), the implicit sixth-order filtering of the upwinded advection scheme is used in place of explicit horizontal mixing, as it is sufficient to dissipate grid-scale energy and enstrophy. Vertical mixing is implemented with the free-tropospheric scheme in the Yonsei University boundary layer model (Noh et al. 2003; note, however, that the boundary layer part of the model is turned off). To minimize gravity wave reflection off the upper boundary, Rayleigh damping is applied to the vertical velocity in the upper 5 km of the model domain (Klemp et al. 2008). Fields are saved every three hours for diagnostics.

3. Overview of simulations

The evolution of the baroclinic life cycle is illustrated by the time series of mass-weighted average eddy kinetic energy (EKE), Fig. 2:

$$\mathrm{EKE} = \iiint \frac{1}{2}\rho(u'^2 + v'^2 + w'^2)\, dV \Big/ \iiint \rho\, dV, \qquad (1)$$

where integration is over the model domain and prime denotes fluctuation from zonal average. Over the first 2 days, the amplitude of the baroclinic wave grows exponentially with a time scale of around 35 h; the EKE of the dry and moist runs are indistinguishable over these early times. After 2 days, the growth rates of the moist waves are slightly enhanced compared to the dry case, as seen in previous studies of moist baroclinic waves (e.g., Gutowski et al. 1992). The maximum rate of EKE injection occurs around $t \approx 4$ days, and is between 3×10^{-4} (dry) and 4×10^{-4} (RH50) $m^2\ s^{-3}$. However, despite these differences, the initial evolution of the EKE is remarkably similar. The baroclinic instability saturates around $t \approx 5$ days. The maximum EKE is similar in the dry and RH30 cases and around 10% higher for RH50.

Condensation first occurs during the second day of evolution for RH50 and a little later for RH30. The precipitation rate (Fig. 3a) increases as the baroclinic instability develops, peaking around the time of maximum EKE and falling off fairly abruptly afterward. In both cases the explicit precipitation—which includes rainfall from stable ascent—dominates, though there is a significant convective contribution as well. In the RH50

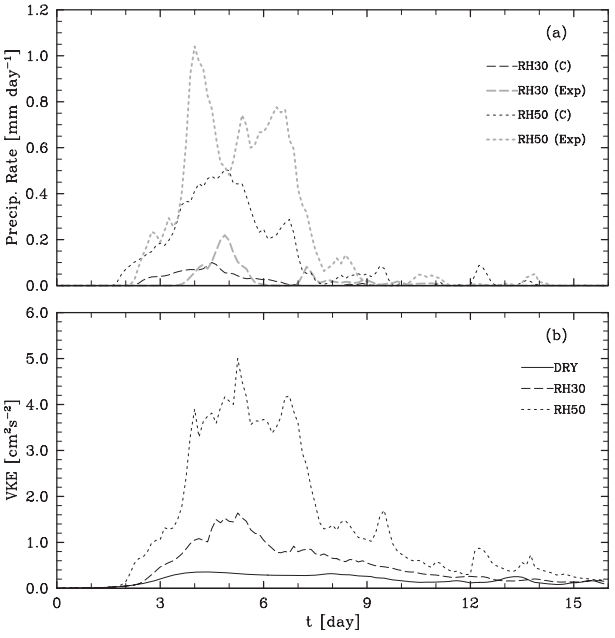

FIG. 3. Time series of the domain-averaged (a) precipitation rate and (b) vertical kinetic energy per unit mass. As in Fig. 2, the vertical kinetic energy is computed with a mass-weighted average. The precipitation rate is averaged over 3-h intervals and separated into convective (C) and explicit (Exp) contributions.

case, the total precipitation over the course of the simulation is roughly two-thirds explicit and one-third convective. The evolution of the vertical kinetic energy (Fig. 3b) closely follows the precipitation rate, which is consistent with the enhanced vertical motion in the moist runs being tied to latent heating. The peak value of the vertical KE occurs around $t = 5$ days and depends quite strongly on moisture: the maxima are around 0.3, 1.6, and 5 cm^2 s^{-2} for the dry, RH30, and RH50 cases, respectively.

In what follows, we analyze the simulations over three phases of the baroclinic life cycle: early ($4 \le t \le 7$ days), during which the baroclinic instability saturates and the maximum precipitation rate, EKE, and vertical KE occur; intermediate ($7 \le t \le 10$ days), during which the EKE falls off from its peak; and late ($10 \le t \le 13$ days), by which time the precipitation and vertical KE have leveled off. Compared to the dry simulations of WS, these experiments are accelerated due to the larger initial perturbation. The EKE in WS saturated around $t \approx 9$ days, so the present experiments are approximately 4 days ahead.

Snapshots of the vertical vorticity $\zeta = \partial v/\partial x - \partial u/\partial y$ are shown in Fig. 4. Fields from the dry and RH50 simulations are plotted at $z = 7$ km and at $t = 2, 5, 8$, and 11 days, which correspond to the linear instability phase and the three phases of nonlinear evolution defined

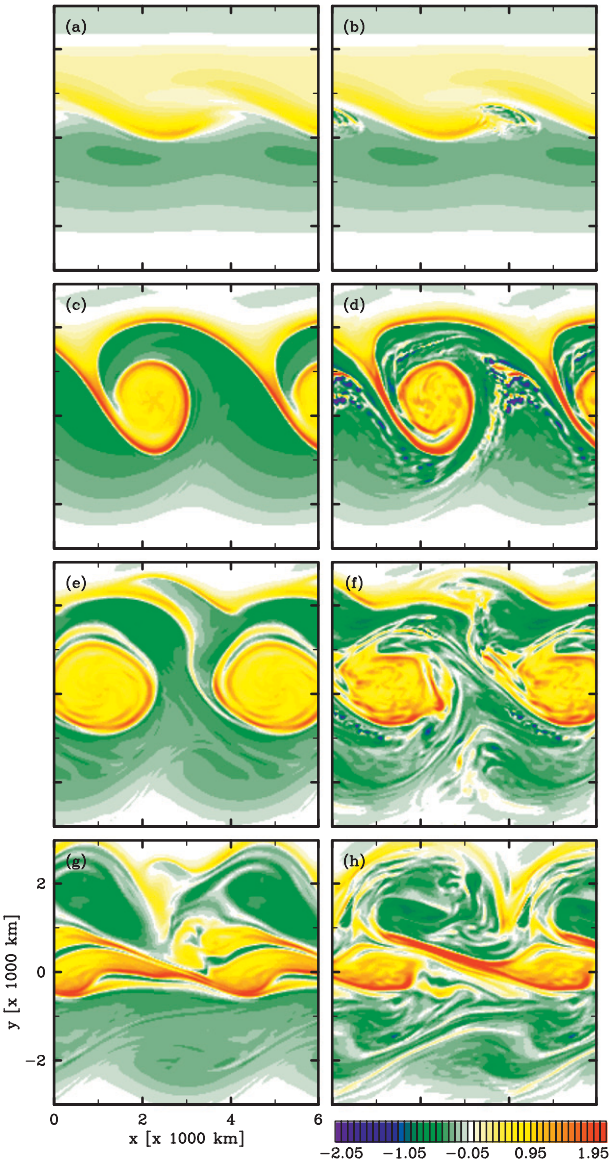

FIG. 4. Vertical vorticity ζ at $z = 7$ km for the (left) dry and (right) RH50 cases at time $t =$ (a),(b) 2, (c),(d) 5, (e),(f) 8, and (g),(h) 11 days. An extra half wavelength is included in x, and the regions within 2000 km of the northern and southern boundaries are omitted. The color map is in units of f, restricted to within $\pm 2f$. However, there are isolated peak values around $\pm 4f$.

above. At $t = 2$ days, the vorticity is very similar in the dry and moist cases, with the exception of a small patch of small-scale fluctuations to the northeast of the developing cyclone in the moist simulation. This feature corresponds to a region of condensation, latent heating, and instability that is not present in the dry experiment. At $t = 5$ days (around the time of the peak precipitation rate), there is strong convection to the east of the cyclone, which leads to localized regions of increased small-scale vorticity in the moist run that are not present in the dry

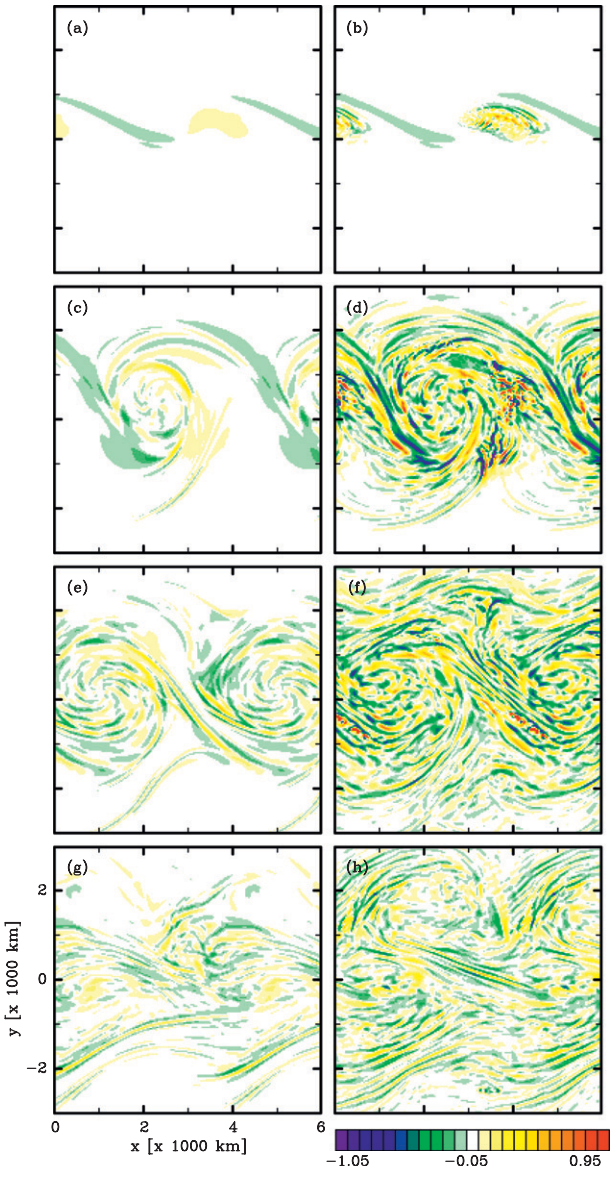

FIG. 5. As in Fig. 4, but for horizontal divergence δ. For clarity, the range of colors is between $\pm f$, a factor of 2 smaller than in Fig. 4. The peak values of δ are around $\pm 2f$. The setup of the plot domain is as in Fig. 4.

simulation. The large-scale vorticity structure, however, is similar in the moist and dry cases. By $t = 8$ days, the differences between the dry and moist vorticity are more significant. At other levels (not shown), the differences between the moist and dry simulation vorticity fields are more pronounced. The instability of the moist cyclone evident in Fig. 4c is much stronger at low levels, while at upper levels anticyclonic vorticity in the moist simulation is enhanced by divergence from convective outflow.

The horizontal divergence $\delta = \partial u/\partial x + \partial v/\partial y$ is plotted in Fig. 5 for the same times and levels as the vorticity. The divergence exhibits a much more significant dependence on moisture than the vorticity. At $t = 2$ h, the dry and moist divergence is similar apart from the patch of instability described above. By $t = 5$ h, there are localized patches of strong divergence in the convective region, as seen in the vorticity. However, by contrast to the vorticity field, the divergence in the moist simulation is greatly amplified over the entire region of the baroclinic wave. In the lower stratosphere, the divergence field is well developed in the moist simulations by this time, but is almost nonexistent in the dry case (not shown). The divergence field in the moist simulation is consistent with IGWs being generated by convection and propagating throughout the large-scale flow of the baroclinic wave. The enhanced divergence of the moist case continues at later times, though it becomes less pronounced by $t = 11$ days.

4. Energy spectra

a. Horizontal wavenumber spectra

Horizontal kinetic energy spectra are computed with two-dimensional discrete Fourier transforms (DFTs) of the horizontal velocity $\mathbf{u} = (u, v)$ on model levels. The zonal transform is natural, as fields are periodic in x; the meridional transform is performed after extending the fields in y (odd extension for v, even extension for other variables) to make them $2L_y$ periodic. Let $\hat{q}(\mathbf{k})$ be the DFT of field q, where $\mathbf{k} = (k_x, k_y)$ is the horizontal wave vector. The horizontal kinetic energy per unit mass associated with wave vector $\mathbf{k}$ at a given time and vertical level is then

$$E(\mathbf{k}) = \frac{1}{2}[\hat{u}(\mathbf{k})\hat{u}(\mathbf{k})^* + \hat{v}(\mathbf{k})\hat{v}(\mathbf{k})^*], \tag{2}$$

where the asterisk denotes complex conjugate and the dependence on z and t has been suppressed for clarity. This approach allows a natural decomposition of the spectrum into horizontally rotational and divergent kinetic energy, given by

$$E_R(\boldsymbol{k}) = \frac{1}{2}\frac{\hat{\zeta}(\mathbf{k})\hat{\zeta}(\mathbf{k})^*}{k_h^2}, \quad E_D(\mathbf{k}) = \frac{1}{2}\frac{\hat{\delta}(\mathbf{k})\hat{\delta}(\mathbf{k})^*}{k_h^2}, \tag{3}$$

where $k_h = |\mathbf{k}|$ is the total horizontal wavenumber. Below we also consider the spectrum of potential temperature variance

$$\Theta(\mathbf{k}) = \frac{1}{2}\hat{\theta}(\mathbf{k})\hat{\theta}(\mathbf{k})^*, \tag{4}$$

which is approximately proportional to the potential energy spectrum when the moist contributions to buoyancy are neglected.

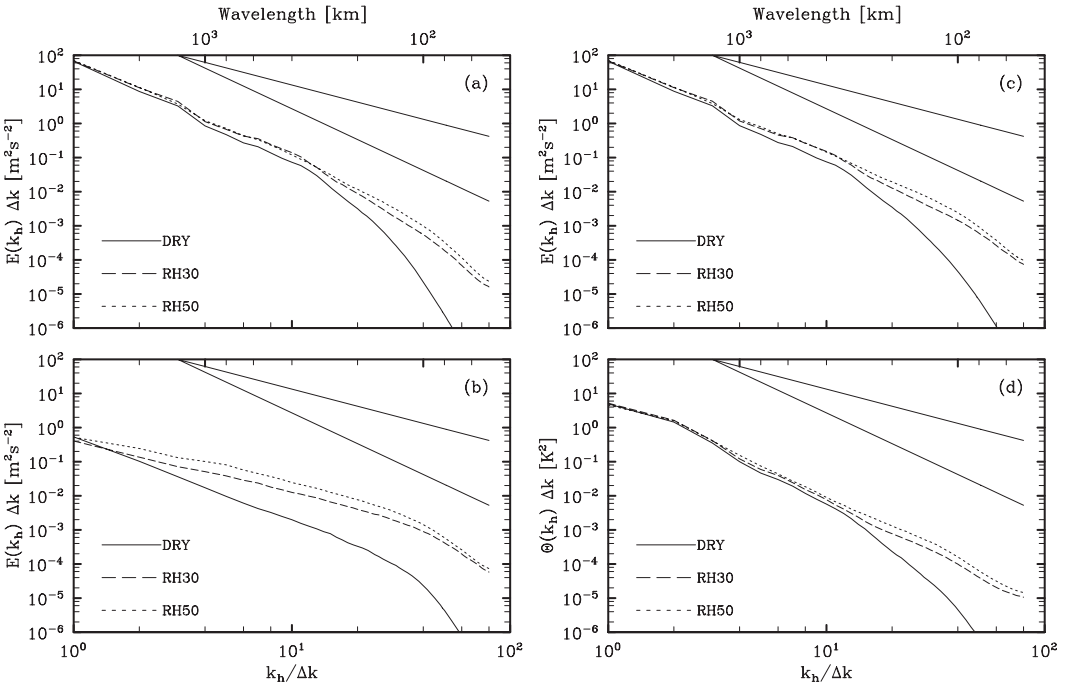

FIG. 6. Horizontal wavenumber spectra of (a) rotational, (b) divergent, and (c) total kinetic energy per unit mass and (d) potential temperature variance, averaged in time over $4 \le t \le 7$ days and in the vertical over $5 \le z \le 10$ km. The solid reference lines have slopes of $-5/3$ and -3.

Given the two-dimensional modal spectra (2) and (3), one-dimensional k_h spectra are computed by summation over circular bands of constant $|\boldsymbol{k}|$ on the k_x–k_y plane (as in, e.g., Waite and Bartello 2004; WS); that is,

$$E(k_h)\Delta k = \sum_{k_h-\Delta k/2 \le k_h' < k_h+\Delta k/2} E(\boldsymbol{k}), \qquad (5)$$

where the k_h bands have width $\Delta k = 2\pi/L_x$. Spectra are also averaged in the vertical over the upper troposphere, $5 \le z \le 10$ km, and in time over the phases described above.

The k_h spectra at early times ($4 \le t \le 7$ days), shown in Fig. 6, are decomposed into rotational and divergent contributions. The RKE spectrum (Fig. 6a) for the dry case resembles a -3 power law for $k_h/\Delta k \lesssim 10$ (i.e., wavelengths larger than around 400 km) and falls off rapidly at larger wavenumbers. The addition of moisture increases the RKE at these larger wavenumbers, leading to a -3 power law extending all the way out to $k_h/\Delta k \approx 40$ for both RH30 and RH50. The slope of the RH50 spectrum in Fig. 6a (measured here and elsewhere by a least squares fit over $4 \le k_h/\Delta k \le 20$) is -3.1. The RH50 case has somewhat more RKE than RH30, but in general the moist spectra are much closer to one another than they are to the dry spectrum. At small wavenumbers with $k_h/\Delta k \lesssim 10$, the dry and moist RKE spectra are remarkably similar; it appears that moisture does not significantly energize the rotational flow at scales larger than ~400 km over $5 \le z \le 10$ km. The potential temperature spectra (Fig. 6d) closely resemble those of RKE at these times with an approximately -3 power law and moist enhancement restricted to small horizontal scales.

The DKE spectra at early times (Fig. 6b) exhibit a much stronger dependence on humidity than the rotational spectra. Moisture energizes the divergent motions of the mesoscale, yielding DKE values that are an order of magnitude larger than in the dry case. For example, the DKE at $k_h/\Delta k = 10$ of RH30 and RH50 are 6 and 13 times larger than the dry simulation, respectively; this gap widens as one moves downscale through the mesoscale. Furthermore, the DKE spectra in the moist simulations are shallower than the dry case with both moist spectra resembling a $-5/3$ power law. The slope of the RH50 spectrum in Fig. 6b is -1.7. The increased kinetic energy in the moist runs—at small scales in the rotational part, and throughout the mesoscale in the divergent part—yields a total mesoscale KE spectrum that is shallower and more energetic than in the dry case (Fig. 6c). In both dry and moist simulations, the total kinetic energy spectrum is dominated by the rotational part (Fig. 7). However, for RH50, the DKE exceeds the RKE for

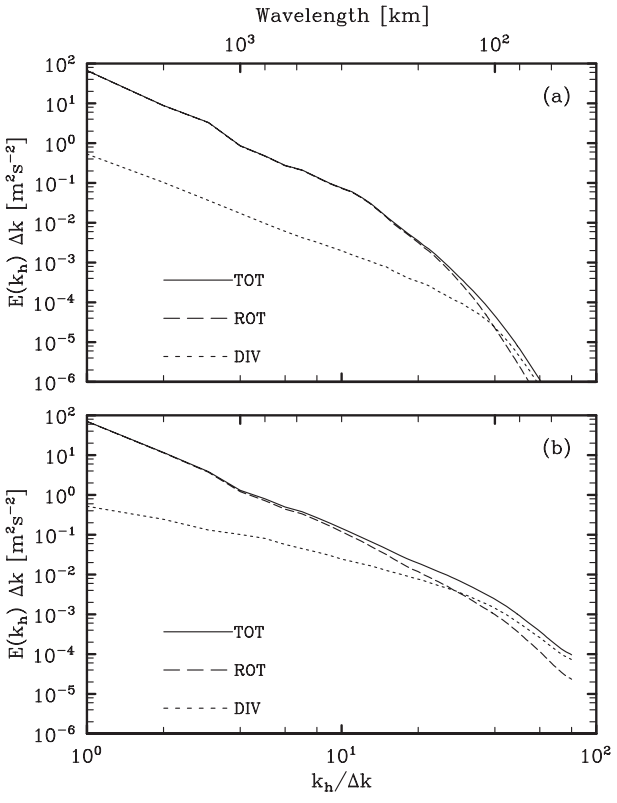

FIG. 7. Horizontal wavenumber spectra of total, rotational, and divergent kinetic energy for the (a) dry and (b) RH50 cases, averaged in time over $4 \le t \le 7$ days: other details as in Fig. 6.

scales below around 100 km, yielding a subtle kink in the spectrum.

The relationship between the spectra and moisture described above persists at later times, though the differences between the dry and moist simulations become somewhat less pronounced. The spectra at intermediate times ($7 \le t \le 10$ days) are shown in Fig. 8. As above, the RKE spectra (Fig. 8a) are close to a -3 power law from large scales down through the mesoscale. The moist cases have slightly more energy than the dry run, particularly at the largest wavenumbers, but overall the spectra are quite insensitive to moisture. Interestingly, there is almost no discernible difference between the RKE spectra of the two moist simulations by this time. The DKE spectra (Fig. 8b) of the dry and moist simulations have similar spectral slopes, but the moist simulations have higher amplitudes. At $k_h/\Delta k = 10$, the DKE of the RH30 and RH50 cases are 3 and 5 times larger than the dry case, respectively; this is a smaller difference than at earlier times, but still significant. The dependence of the temperature spectra (Fig. 8d) on moisture continues to be restricted to small scales, where moist enhancement yields a kink in the spectrum around $k_h/\Delta k \gtrsim 10$. The story is much the same at later times (Fig. 9), although the difference between the dry and moist DKE is even smaller, as the moist DKE appears to decay more rapidly than the dry.

b. Zonal wavenumber spectra

The tendency of moisture to energize the mesoscale puts the moist spectra in better agreement with observations than the dry simulation. One-dimensional zonal wavenumber (k_x) KE spectra are plotted in Fig. 10 over the early phase when moist effects are strongest. These spectra are computed from one-dimensional velocity transects at fixed y and z, and are averaged in y over the most active part of the domain (we use $-L_y/8 \le y \le L_y/4$ since the peak divergence is centered slightly north of the centerline at these times; see, e.g., Fig. 5d). As for the k_h spectra above, the moist simulations have a more energetic mesoscale with a shallower slope than the dry case. Also plotted in Fig. 10 is the reference one-dimensional spectrum from Lindborg (1999), which was obtained from a fit to Measurement of Ozone and Water Vapor by Airbus In-Service (MOZAIC) data and is a linear combination of a -3 and $-5/3$ power law at large and small scales, respectively. As found in WS, the dry simulation has significantly less mesoscale energy than the reference curve. The inclusion of moisture, however, leads to a reasonable agreement between our simulations and the data, at least down to zonal scales of around 400 km ($k_x/\Delta k \approx 10$).

5. Moist forcing

a. Buoyancy flux and latent heating spectra

Moist processes influence the kinetic energy spectrum via their effects on buoyancy. Phase changes of water modify the density of moist air by latent heating and cooling, as well as (to a lesser extent) through the direct dependence of the density on humidity. These effects in turn can enhance the buoyant production of kinetic energy. In the spectral energy budget, buoyant production of KE appears as the cross spectrum of buoyancy and vertical velocity [the buoyancy flux; e.g., Holloway 1988; WS, Eq. (13)], which for a given wave vector $\mathbf{k}$ can be expressed as

$$B(\mathbf{k}) = \frac{1}{2}\frac{g}{\overline{\alpha}}\hat{w}^*(\mathbf{k})\hat{\alpha}'(\mathbf{k}) + \text{c.c.}, \tag{6}$$

where α is the specific volume of moist air, $\overline{\alpha}$ is a background profile, prime denotes fluctuation from the background, and c.c. is complex conjugate. We calculate the buoyancy field using specific volume fluctuations because $\overline{\alpha}$ is readily available in WRF (buoyancy flux

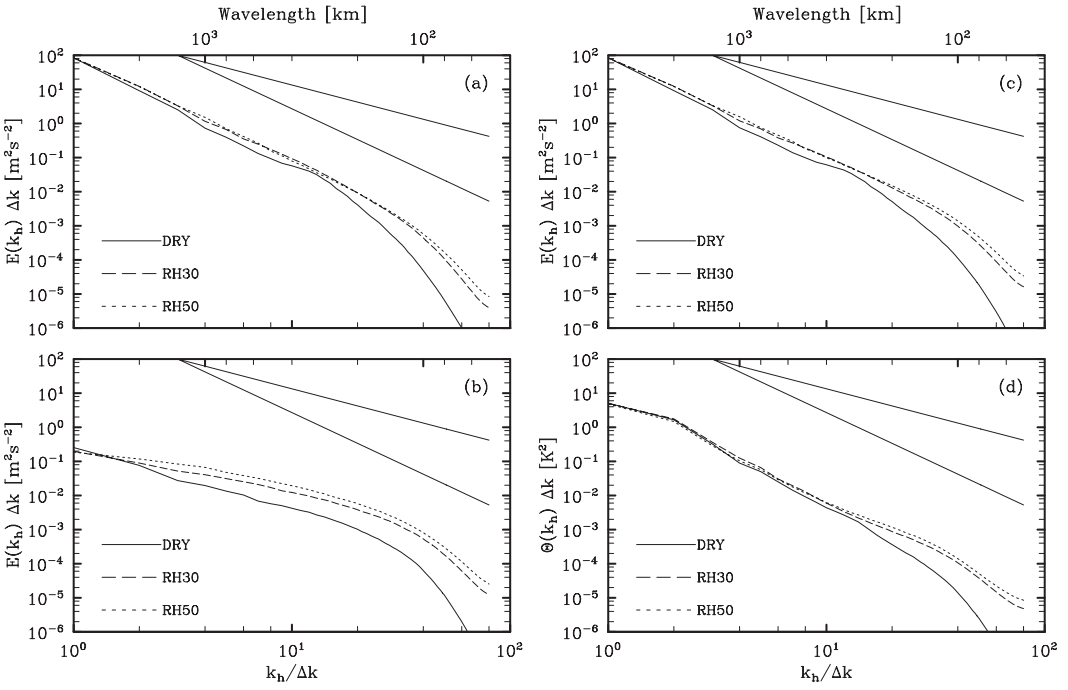

FIG. 8. Horizontal wavenumber spectra of (a) rotational, (b) divergent, and (c) total kinetic energy per unit mass and (d) potential temperature variance, averaged in time over $7 \le t \le 10$ days: other details as in Fig. 6.

spectra computed with virtual potential temperature fluctuations are nearly identical in the mesoscale). Positive $B(\mathbf{k})$ implies a positive conversion of available potential to kinetic energy at wave vector $\mathbf{k}$. Horizontal spectra $B(k_h)$ are computed as outlined in (5).

Horizontal buoyancy flux spectra for the dry and moist simulations are shown in Fig. 11. Spectra are averaged over the early phase of the simulations, where precipitation—and, as it turns out, the mesoscale buoyancy flux—is strongest. The buoyancy flux is dominated by the largest scales (Fig. 11a), which exhibit a net exchange from potential to kinetic energy at wavenumber one for both dry and moist cases, consistent with the baroclinic instability at this scale. The mesoscale buoyancy flux (magnified in Fig. 11b) has a very strong dependence on moisture. In the dry simulation there is a weak, negative mesoscale $B(k_h)$, similar to what was found in WS. The moist simulations, by contrast, exhibit a much larger and positive $B(k_h)$ throughout the mesoscale. In the RH50 case, the buoyancy flux spectrum is characterized by a peak around $k_h/\Delta k = 5$ corresponding to length scales of 800 km, that is, the outer end of the mesoscale range. In addition, there is a smaller positive $B(k_h)$ over the rest of the mesoscale. The structure of the RH30 spectrum is similar—there is a peak around $k_h/\Delta k \approx 8$ along with smaller positive tail at larger k_h—but the amplitude is smaller than in the RH50 case.

The forcing of the kinetic energy spectrum by buoyancy flux in the moist simulations is significant. In RH50, the ratio of $E(k_h)$ to $B(k_h)$ at $k_h/\Delta k = 5$ is around 12 h, comparable to the nonlinear time scale of the baroclinic wave, which was shown in WS to be around 1 day. [Koshyk and Hamilton (2001) found similarly strong buoyancy flux across a wide range of scales in their simulations.] Furthermore, the total mesoscale buoyancy flux, that is, the integral of $B(k_h)$ for $k_h/\Delta k \ge 4$, is 6.5×10^{-5} m^2 s^{-3}: this is the average rate at which kinetic energy is being converted from potential energy in the upper troposphere over the early phase of this simulation, and is ~20% of the maximum rate of EKE injection by the baroclinic instability. A large fraction of the mesoscale flux comes from the outer mesoscale peak: the integrated buoyancy flux over $4 \le k_h/\Delta k \le 7$ is 2.5×10^{-5} m^2 s^{-3}, or roughly 40% of the total. To put this value into context, the average KE dissipation rate in the upper troposphere has been computed to be $\epsilon = 6 \times 10^{-5}$ m^2 s^{-3} (Lindborg and Cho 2001).

The ultimate source of the enhanced buoyancy flux in the moist simulations is latent heating. Its effect on the θ spectrum can be found by computing the cross spectrum of the heating field and potential temperature:

$$F(\boldsymbol{k}) = \frac{1}{2}\hat{\theta}^*(\mathbf{k})\hat{H}(\mathbf{k}) + \text{c.c.} \qquad (7)$$

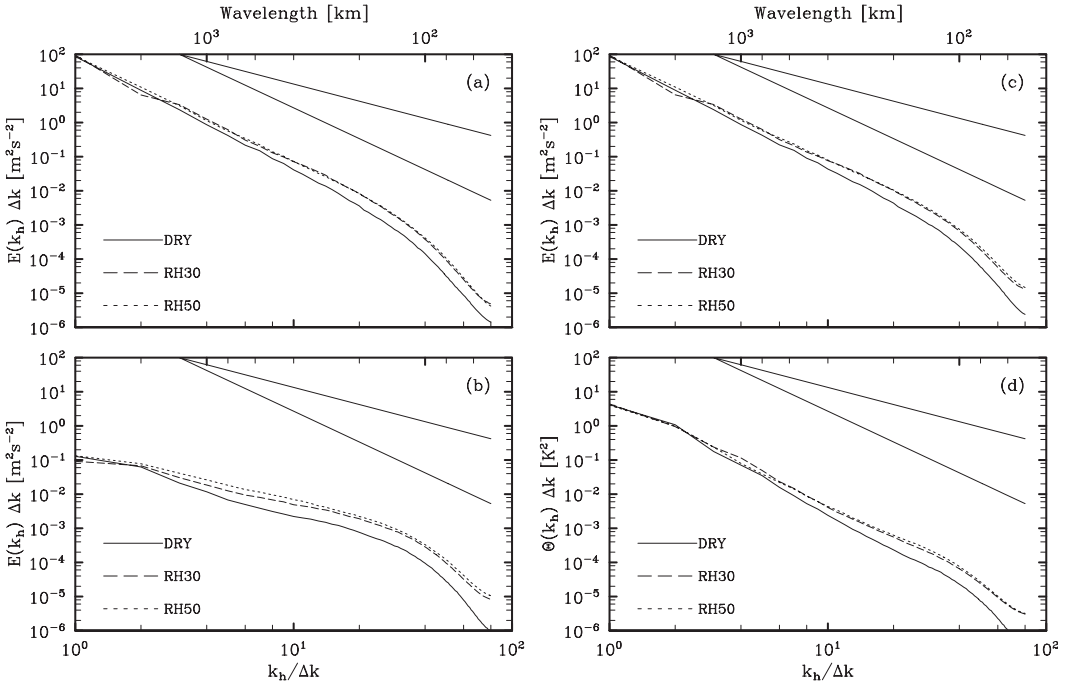

FIG. 9. As in Fig. 8, but averaged in time over $10 \le t \le 13$ days.

Here, H is the potential temperature tendency due to moist physics, which has two contributions: explicit latent heating from the microphysical parameterization and heating from unresolved convection in the cumulus scheme. The spectrum in (7) appears as a source term in the equation for $\Theta(\mathbf{k})$ and is plotted in Fig. 12 for the RH50 case, averaged over the early phase of the simulation. It has much the same structure as the buoyancy flux in Fig. 11. There is a negative peak at $k_h/\Delta k \approx 2$, signifying that heating at these large scales is predominantly in regions of negative θ anomalies. There is also a local maximum around wavenumber 5, which is consistent with the large-scale organization of latent heating by the baroclinic wave. In addition, there is a broad range of positive heating throughout the mesoscale. Over all scales, the heating is dominated by the microphysical contribution.

b. Relaxation to dry dynamics

The direct forcing of mesoscale KE by positive buoyancy flux accounts for the enhanced divergent spectrum in the moist simulations at early times when latent heating is strongest. But for how long does this effect persist? The spectra from the late period $10 \le t \le 13$ days (Fig. 9) show that, even several days after the maximum heating, the moist simulations have more mesoscale divergent kinetic energy than the dry case. To investigate this question further, we have performed an additional experiment in which the RH50 case is restarted at $t = 5$ days with latent heating turned off. This simulation was run for three days to analyze the time scale over which the mesoscale loses DKE in the absence of heating.

Two days after the latent heating is turned off, the mesoscale DKE spectrum is clearly reduced relative to the full RH50 run (Fig. 13a). The RH50 spectrum at this time has a broad bulge in the mesoscale, consistent with direct forcing at these scales; the simulation without heating, by contrast, is closer to a $-5/3$ power law. Even

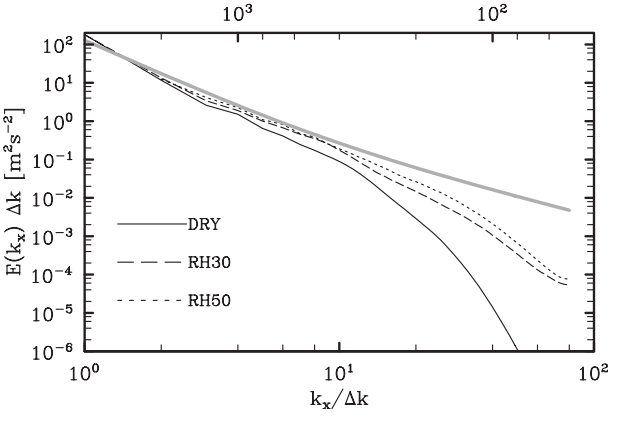

FIG. 10. Zonal wavenumber spectra of kinetic energy per unit mass, averaged in time over $4 \le t \le 7$ days, in the vertical over $5 \le z \le 10$ km and in y over $-L_y/8 \le y \le L_y/4$. The smooth gray line is the reference spectrum from Lindborg (1999).

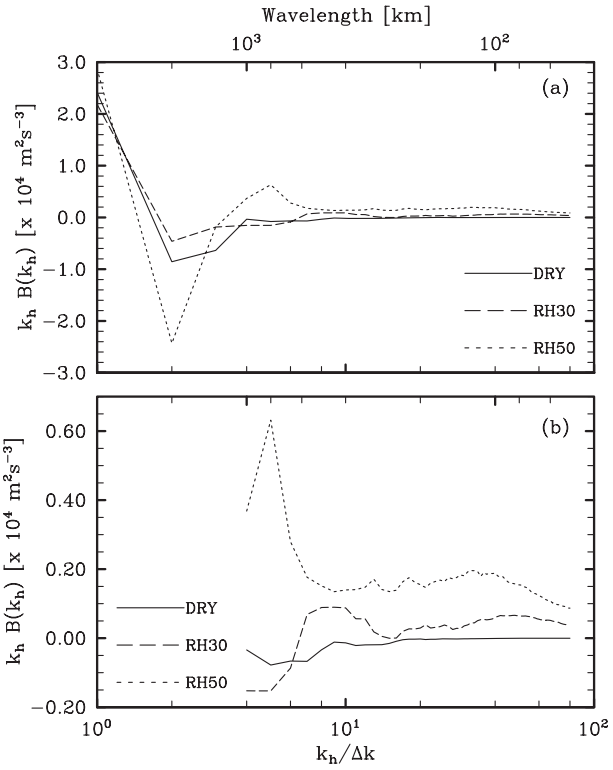

FIG. 11. Horizontal wavenumber buoyancy flux spectra, averaged in time over $4 \le t \le 7$ days and in the vertical over $5 \le z \le 10$ km: (a) shows the full range of values, while (b) is zoomed in to emphasize the mesoscale subrange $k/\Delta k \ge 4$. For clarity, the buoyancy flux is multiplied by k_h, which preserves area on a log-linear plot.

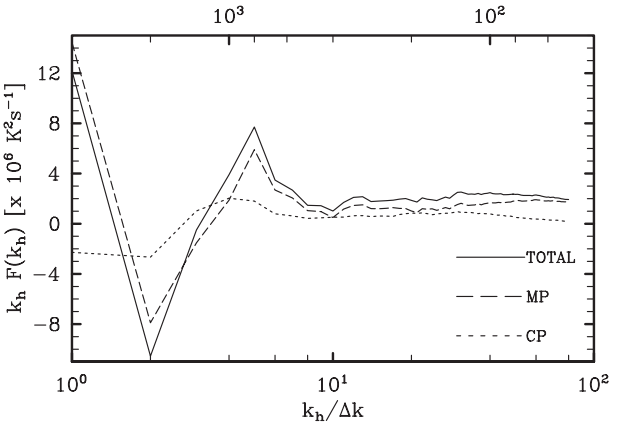

FIG. 12. Horizontal wavenumber heating spectra for the RH50 case, averaged in time over $4 \le t \le 7$ days and in the vertical over $5 \le z \le 10$ km. The total is shown as well as contributions from the microphysical (MP) and convective (CP) parameterizations. For clarity, the spectra are multiplied by k_h, which preserves area on a log–linear plot.

2 days after the heating is stopped, the experiment without heating still has significantly more mesoscale DKE than the full dry case. The decay of mesoscale DKE is illustrated in Fig. 13b, which shows a time series of DKE in a wavenumber band of width $2\Delta k$ around $k_h/\Delta k = 10$. After latent heating is stopped at $t = 5$ days, the DKE decreases. The decay is approximately exponential with an *e*-folding time scale of around 2.3 days, similar to the nonlinear time scale of the baroclinic wave. By contrast, the full RH50 simulation has approximately constant mesoscale DKE, while the dry case has small but increasing energy, over the same time period.

6. Sensitivity

The moist simulations presented here are not significantly dependent on our choices of convective and microphysics parameterizations. To verify robustness, we have repeated the RH50 case with three different parameterization configurations: with the Kain and Fritsch (1990) cumulus scheme in place of the Betts–Miller–Janjić scheme, with no convection scheme, and with WRF single-moment 5-class (WSM5) microphysics (Hong et al. 2004) in place of the Kessler scheme. Rotational and divergent KE and buoyancy flux spectra from these sensitivity experiments are shown in Fig. 14. Spectra are compared over the early phase $4 \le t \le 7$ days, when convection is strongest. The energy and buoyancy flux spectra are quite insensitive to the choice of parameterization. The only exception is the simulation run without any convection scheme, which is slightly overenergized at large wavenumbers ($k_h/\Delta k \gtrsim 20$, corresponding to scales smaller than around 200 km). This behavior appears to result from excessive small-scale buoyancy flux, likely due to spuriously strong grid-scale heating. The grid spacing here is probably too coarse to be run without a convection scheme, but even this simulation does remarkably well at scales larger than 400 km. The minor differences between the spectra in Fig. 14 are even less pronounced at later times (not shown).

We have also verified the robustness of these results to the numerical grid spacing by repeating the RH50 simulation with a higher horizontal resolution of $\Delta x = 12.5$ km and a higher vertical resolution of 360 levels ($\Delta z \approx 55$ m in troposphere). Over the range of scales resolved by the control run ($k_h/\Delta k \lesssim 30$), the spectra of rotational and divergent KE are essentially unaffected by the doubling of horizontal or vertical resolution (Fig. 14, results at later times are also insensitive). The positive tail in the higher-horizontal-resolution buoyancy flux is shifted downscale somewhat relative to the control run, but the total KE injected from the large- and small-scale ends of the mesoscale is approximately unchanged. This finding confirms, in particular, that the amplitude of the divergent

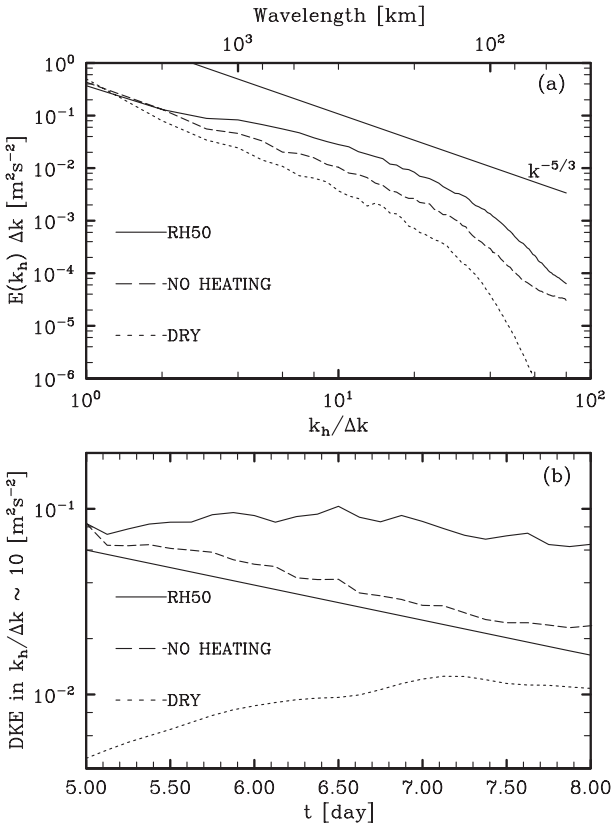

FIG. 13. (a) Horizontal wavenumber spectra of divergent kinetic energy at $t = 7$ days for the RH50 case, the experiment with no latent heating, and the dry simulation: other details as in Fig. 6. (b) Time series of divergent kinetic energy in the wavenumber range $9 \leq k_h/\Delta k \leq 11$ for the same three simulations as in (a). The solid reference curve is exponential decay with an *e*-folding time of 2.3 days.

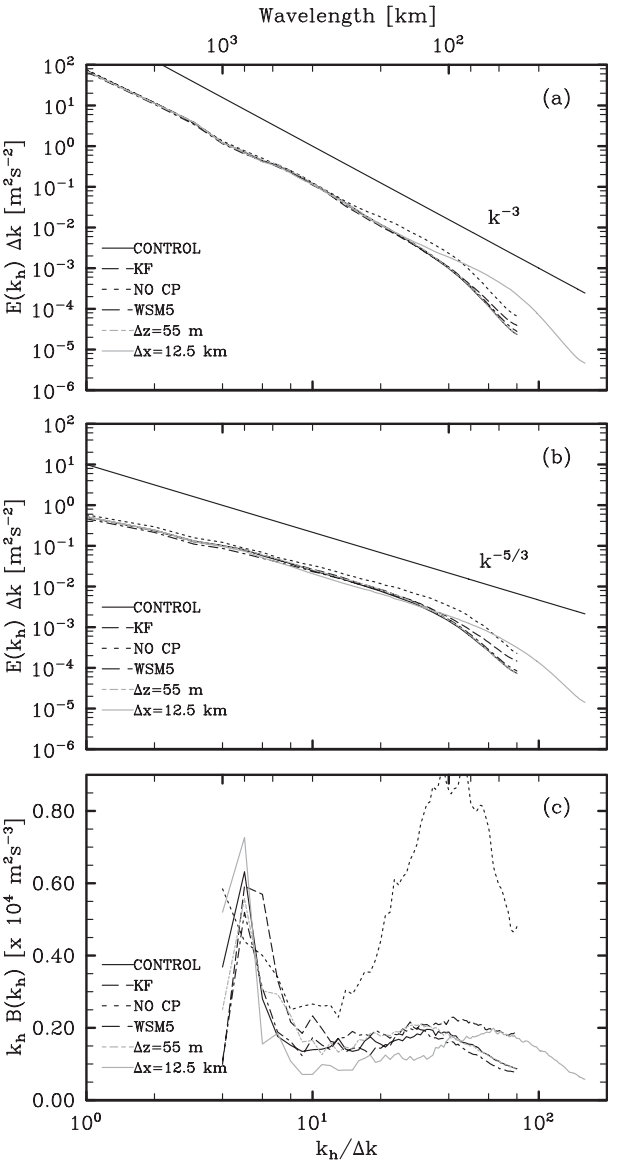

FIG. 14. Horizontal wavenumber spectra of (a) rotational kinetic energy, (b) divergent kinetic energy, and (c) buoyancy flux in the RH50 case for the control run and sensitivity tests with different parameterizations and resolutions: Kain–Fritsch convection (KF), no explicit convection scheme (NO CP), WSM5 microphysics, double vertical resolution ($\Delta z \approx 55$ m), and double horizontal resolution ($\Delta x \approx 12.5$ km). Spectra are averaged in time over $4 \leq t \leq 7$ days and in the vertical over $5 \leq z \leq 10$ km: other details as in Figs. 6 and 11.

KE spectrum is not an artifact of the grid resolution in these simulations. Interestingly, the rotational KE spectrum in the high-horizontal-resolution simulation shallows at scales of ~100 km, below which DKE ≈ RKE (Fig. 15). This finding suggests that the RKE spectrum may follow the more shallow DKE at small scales in even higher-resolution simulations.

7. Conclusions

Numerical simulations of moist baroclinic life cycles have been presented as an idealized framework for studying the effects of moisture on energy transfers through the upper-tropospheric mesoscale. These simulations show that the inclusion of moisture can have a very strong impact on the mesoscale kinetic energy spectra of baroclinic waves, as found in the global model simulations of Hamilton et al. (2008). In both moist and dry simulations the total kinetic energy is dominated by the rotational part of the spectrum, which has an approximately −3 power law. Moist processes primarily enhance the divergent part of the spectrum, which has a relatively shallow spectral slope that resembles $-5/3$. At lowest order this spectrum approximates the kinetic energy of inertia–gravity waves. The amplitude of the DKE spectrum is very sensitive to humidity; moist simulations

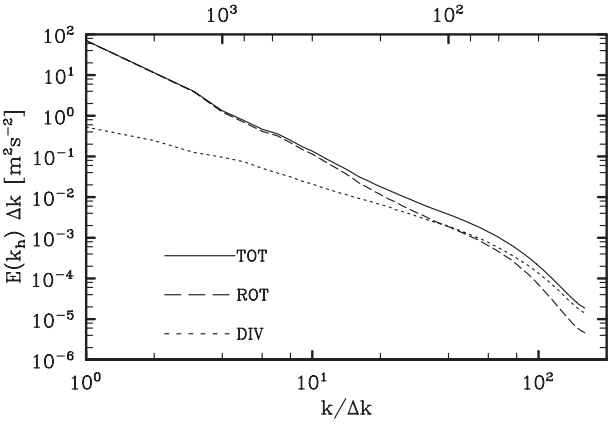

FIG. 15. Horizontal wavenumber spectra of total, rotational, and divergent kinetic energy for the RH50 case with $\Delta x = 12.5$ km. Spectra are averaged in time over $4 \le t \le 7$ days and in the vertical over $5 \le z \le 10$ km.

can have amplitudes that are an order of magnitude larger than those in the dry case. The differences between the dry and moist spectra are greatest at the times of strongest precipitation and latent heating, but they persist well into the mature evolution of the baroclinic wave.

The moist simulations have significant mesoscale buoyancy flux, which corresponds to a positive conversion of potential to kinetic energy. Latent heating generates temperature, and hence buoyancy, perturbations, which ultimately inject KE into the system. We have shown that the moist simulations have positive buoyancy flux and generation of potential energy by heating at mesoscale length scales. Over the period of maximum heating, the buoyancy flux spectrum in the RH50 simulation has a peak at scales of around 800 km and a broad tail throughout the mesoscale. The total resulting forcing of KE is significant, and is roughly evenly split between the peak and the tail. Even if the latent heating is abruptly stopped, the enhanced DKE takes several days to relax to the lower levels obtained in the dry simulation.

Despite the idealized configuration of these experiments, the ratio of DKE to RKE in our moist simulations is in the range of that found in previous investigations of the mesoscale spectrum (e.g., Lindborg 2007; Hamilton et al. 2008; Skamarock and Klemp 2008); in the RH50 case at early times, we have DKE/RKE $\gtrsim$ 1/3 for scales below around 300 km. As in these studies, the large-scale end of the mesoscale is characterized by RKE and DKE spectral slopes of around -3 and $-5/3$, respectively. In our highest-resolution RH50 simulation, there is a suggestion of a transition at scales of around 100 km, below which the RKE spectrum shallows and RKE $\approx$ DKE, but higher-resolution simulations are required to investigate the scaling in this range. This transition scale is similar to that found in Lindborg (2007), but is a few times smaller than the transition in Hamilton et al. (2008) and Skamarock and Klemp (2008), which was found to be around 400–500 km.

These simulations suggest the following hypothesis for how moisture enhances the upper-tropospheric mesoscale. Latent heating creates strong buoyancy perturbations that excite inertia–gravity waves. The wave source is localized in space and appears strongest to the northeast of the developing vortex. However, the excited waves quickly propagate away from the heating and throughout the balanced vortical flow of the baroclinic wave. As they propagate through the large-scale strain field, their horizontal wavelengths contract [as described by Plougonven and Snyder (2005)], and their energy is transferred to smaller horizontal scales. This process is reminiscent of the resonant triad interaction of two IGWs with a balanced vortex mode, in which the vortex catalyzes the transfer of energy from large- to small-wavelength IGWs (Lelong and Riley 1991; Bartello 1995). Numerical simulations (Bartello 1995) and phenomenological arguments (Babin et al. 1997) suggest that the spectrum of wave energy resulting from such interactions has a slope in the range of -1 to -2, which is in line with our findings.

These simulations have implications for the various cascade theories that have been proposed to explain the mesoscale energy spectrum. The idealization of the mesoscale as an inertial subrange requires that there be no significant mesoscale forcing or damping of kinetic energy. Our moist simulations have a peak injection of KE at the large-scale end of the mesoscale, which is consistent with an inertial subrange at smaller scales (i.e., scenario 1 from the introduction). However, the broad tail of positive buoyancy flux in these simulations implies that there is also significant direct forcing of the mesoscale (i.e., scenario 2). Any comprehensive theory for the mesoscale spectrum should account for the presence of intermittent but very broad band forcing of the mesoscale by latent heating.

The simulations presented here clearly demonstrate the importance of moist processes in establishing the mesoscale spectrum of divergent kinetic energy. In the moist simulations, buoyancy flux injects kinetic energy throughout the mesoscale at a rate comparable to the observed dissipation rate. The inclusion of moist processes helps to close the gap between the baroclinic wave mesoscale and observations; indeed, the moist spectra here are in much better agreement with the Lindborg (1999) reference spectrum than the dry experiments of WS.

Even with moisture, however, the mesoscale spectra of total kinetic energy in our experiments have lower

amplitudes than what is observed, particularly below scales of ~400 km. Furthermore, they do not exhibit the expected shallowing of total kinetic at scales of ~400 km that characterizes the Nastrom and Gage (1985) spectrum. This discrepancy with observations does not seem to result from numerical dissipation or errors; our setup is standard, our vertical resolution is exceptionally high, and sensitivity tests show robustness to resolution and moist parameterizations. While it would of course be desirable to verify our findings with cloud-resolving simulations, our results give no indication that such high resolution would change the conclusions (although we anticipate that the transition to a flatter spectrum, which begins in Fig. 15 for the $\Delta x \approx 12.5$ km simulation at a wavelength somewhat less than 200 km, would be more apparent).

Thus, while the basic mechanism of our experiments, by which latent heating in moist baroclinic waves energizes the mesoscale, will almost certainly be present in more comprehensive simulations (and indeed in the real midlatitude atmosphere), it is equally clear that some processes important to the atmospheric energy spectrum are missing from our idealized simulations. It is possible that a forced–dissipative setup, with radiative forcing and surface fluxes continually injecting energy, would allow the mesoscale spectrum to build up to higher levels in better agreement with observations.

Acknowledgments. High-performance computing support was provided by NCAR's Computational and Information Systems Laboratory, sponsored by the National Science Foundation. Some computations were also performed on the General Purpose Cluster supercomputer at the SciNet HPC Consortium. SciNet is funded by the Canada Foundation for Innovation under the auspices of Compute Canada, the Government of Ontario, Ontario Research Fund Research Excellence, and the University of Toronto. MLW acknowledges funding from the Natural Sciences and Engineering Research Council of Canada.

REFERENCES

Babin, A., A. Mahalov, B. Nicolaenko, and Y. Zhou, 1997: On the asymptotic regimes and the strongly stratified limit of rotating Boussinesq equations. *Theor. Comput. Fluid Dyn.,* **9,** 223–251.

Bartello, P., 1995: Geostrophic adjustment and inverse cascades in rotating stratified turbulence. *J. Atmos. Sci.,* **52,** 4410–4428.

——, 2010: Quasigeostrophic and stratified turbulence in the atmosphere. *Proc. IUTAM Symp. on Turbulence in the Atmosphere and Oceans,* Cambridge, United Kingdom, IUTAM, 117–130.

Betts, A. K., and M. J. Miller, 1986: A new convective adjustment scheme. Part II: Single column tests using GATE wave, BOMEX, ATEX and arctic air mass data sets. *Quart. J. Roy. Meteor. Soc.,* **112,** 693–709.

Charney, J. G., 1971: Geostrophic turbulence. *J. Atmos. Sci.,* **28,** 1087–1095.

Cho, J. Y. N., and Coauthors, 1999a: Horizontal wavenumber spectra of winds, temperature, and trace gases during the Pacific Exploratory Missions: 1. Climatology. *J. Geophys. Res.,* **104** (D5), 5697–5716.

——, R. E. Newell, and J. D. Barrick, 1999b: Horizontal wavenumber spectra of winds, temperature, and trace gases during the Pacific Exploratory Missions: 2. Gravity waves, quasi-two-dimensional turbulence, and vortical modes. *J. Geophys. Res.,* **104** (D13), 16 297–16 308.

Davidson, P. A., 2004: *Turbulence: An Introduction for Scientists and Engineers.* Oxford University Press, 678 pp.

Davis, C. A., 2010: Simulations of subtropical cyclones in a baroclinic channel model. *J. Atmos. Sci.,* **67,** 2871–2892.

Dewan, E. M., 1979: Stratospheric wave spectra resembling turbulence. *Science,* **204,** 832–835.

Done, J., C. A. Davis, and M. Weisman, 2004: The next generation of NWP: Explicit forecasts of convection using the Weather Research and Forecasting (WRF) model. *Atmos. Sci. Lett.,* **5,** 110–117.

Gage, K. S., 1979: Evidence for a $k^{-5/3}$ law inertial range in mesoscale two-dimensional turbulence. *J. Atmos. Sci.,* **36,** 1950–1954.

Gkioulekas, E., and K. K. Tung, 2005a: On the double cascades of energy and enstrophy in two dimensional turbulence. Part 1. Theoretical formulation. *Discrete Contin. Dyn. Syst.,* **5B,** 79–102.

——, and ——, 2005b: On the double cascades of energy and enstrophy in two dimensional turbulence. Part 2. Approach to the KLB limit and interpretation of experimental evidence. *Discrete Contin. Dyn. Syst.,* **5B,** 103–124.

Gutowski, W. J., L. E. Branscome, and D. A. Stewart, 1992: Life cycles of moist baroclinic eddies. *J. Atmos. Sci.,* **49,** 306–319.

Hamilton, K., Y. O. Takahashi, and W. Ohfuchi, 2008: The mesoscale spectrum of atmospheric motions investigated in a very fine resolution global general circulation model. *J. Geophys. Res.,* **113,** D18110, doi:10.1029/2008JD009785.

Holloway, G., 1988: The buoyancy flux from internal gravity wave breaking. *Dyn. Atmos. Oceans,* **12,** 107–125.

Hong, S.-Y., J. Dudhia, and S.-H. Chen, 2004: A revised approach to ice microphysical processes for the bulk parameterization of clouds and precipitation. *Mon. Wea. Rev.,* **132,** 103–120.

Janjić, Z. I., 1994: The step-mountain eta coordinate model: Further developments of the convection, viscous sublayer, and turbulence closure schemes. *Mon. Wea. Rev.,* **122,** 927–945.

Kain, J. S., and J. M. Fritsch, 1990: A one-dimensional entraining/detraining plume model and its application in convective parameterization. *J. Atmos. Sci.,* **47,** 2784–2802.

Kessler, E., 1969: *On the Distribution and Continuity of Water Substance in the Atmosphere Circulations. Meteor. Monogr.,* No. 32, Amer. Meteor. Soc., 246 pp.

Kitamura, Y., and Y. Matsuda, 2010: Energy cascade processes in rotating stratified turbulence with application to the atmospheric mesoscale. *J. Geophys. Res.,* **115,** D11104, doi:10.1029/2009JD012368.

Klemp, J. B., J. Dudhia, and A. D. Hassiotis, 2008: An upper gravity-wave absorbing layer for NWP applications. *Mon. Wea. Rev.,* **136,** 3987–4004.

Kolmogorov, A. N., 1941: The local structure of turbulence in incompressible viscous fluid for very large Reynolds number. *Dokl. Akad. Nauk SSSR,* **30,** 301–305.

Koshyk, J. N., and K. Hamilton, 2001: The horizontal kinetic energy spectrum and spectral budget simulated by a high-resolution

troposphere–stratosphere–mesosphere GCM. *J. Atmos. Sci.,* **58,** 329–348.

Kraichnan, R. H., 1967: Inertial ranges in two-dimensional turbulence. *Phys. Fluids,* **10,** 1417–1423.

Lelong, M.-P., and J. J. Riley, 1991: Internal wave-vortical mode interactions in strongly stratified flows. *J. Fluid Mech.,* **232,** 1–19.

Lilly, D. K., 1983: Stratified turbulence and the mesoscale variability of the atmosphere. *J. Atmos. Sci.,* **40,** 749–761.

Lindborg, E., 1999: Can the atmospheric kinetic energy spectrum be explained by two-dimensional turbulence? *J. Fluid Mech.,* **388,** 259–288.

——, 2006: The energy cascade in a strongly stratified fluid. *J. Fluid Mech.,* **550,** 207–242.

——, 2007: Horizontal wavenumber spectra of vertical vorticity and horizontal divergence in the upper troposphere and lower stratosphere. *J. Atmos. Sci.,* **64,** 1017–1025.

——, and J. Y. N. Cho, 2001: Horizontal velocity structure functions in the upper troposphere and lower stratosphere. 2. Theoretical considerations. *J. Geophys. Res.,* **106** (D10), 10 233–10 241.

Nastrom, G. D., and K. S. Gage, 1985: A climatology of atmospheric wavenumber spectra observed by commercial aircraft. *J. Atmos. Sci.,* **42,** 950–960.

Noh, Y., W. G. Cheon, S.-Y. Hong, and S. Raasch, 2003: Improvement of the K-profile model for the planetary boundary layer based on large eddy simulation data. *Bound.-Layer Meteor.,* **107,** 401–427.

O'Sullivan, D., and T. J. Dunkerton, 1995: Generation of inertia–gravity waves in a simulated life cycle of baroclinic instability. *J. Atmos. Sci.,* **52,** 3695–3716.

Plougonven, R., and C. Snyder, 2005: Gravity waves excited by jets: Propagation versus generation. *Geophys. Res. Lett.,* **32,** L18802, doi:10.1029/2005GL023730.

——, and ——, 2007: Inertia–gravity waves spontaneously generated by jets and fronts. Part I: Different baroclinic life cycles. *J. Atmos. Sci.,* **64,** 2502–2520.

Rotunno, R., W. C. Skamarock, and C. Snyder, 1994: An analysis of frontogenesis in numerical simulations of baroclinic waves. *J. Atmos. Sci.,* **51,** 3373–3398.

Skamarock, W. C., 2004: Evaluating mesoscale NWP models using kinetic energy spectra. *Mon. Wea. Rev.,* **132,** 3019–3032.

——, and J. B. Klemp, 2008: A time-split nonhydrostatic atmospheric model for weather research and forecasting applications. *J. Comput. Phys.,* **227,** 3465–3485.

——, and Coauthors, 2008: A description of the Advanced Research WRF version 3. NCAR Tech. Note 475+STR, 113 pp.

Snyder, C., and R. S. Lindzen, 1991: Quasigeostrophic wave-CISK in an unbounded baroclinic shear. *J. Atmos. Sci.,* **48,** 76–86.

——, W. C. Skamarock, and R. Rotunno, 1991: A comparison of primitive-equation and semigeostrophic simulations of baroclinic waves. *J. Atmos. Sci.,* **48,** 2179–2194.

Takahashi, Y. O., K. Hamilton, and W. Ohfuchi, 2006: Explicit global simulations of the mesoscale spectrum of atmospheric motions. *Geophys. Res. Lett.,* **33,** L12812, doi:10.1029/2006GL026429.

Thorpe, A. J., and K. A. Emanuel, 1985: Frontogenesis in the presence of small stability to slantwise convection. *J. Atmos. Sci.,* **42,** 1809–1824.

Tulloch, R., and K. S. Smith, 2009: Quasigeostrophic turbulence with explicit surface dynamics: Application to the atmospheric energy spectrum. *J. Atmos. Sci.,* **66,** 450–467.

Tung, K. K., and W. W. Orlando, 2003: The k^{-3} and $k^{-5/3}$ energy spectrum of atmospheric turbulence: Quasigeostrophic two-level model simulation. *J. Atmos. Sci.,* **60,** 824–835.

VanZandt, T. E., 1982: A universal spectrum of buoyancy waves in the atmosphere. *Geophys. Res. Lett.,* **9,** 575–578.

Waite, M. L., and P. Bartello, 2004: Stratified turbulence dominated by vortical motion. *J. Fluid Mech.,* **517,** 281–308.

——, and C. Snyder, 2009: The mesoscale kinetic energy spectrum of a baroclinic life cycle. *J. Atmos. Sci.,* **66,** 883–901.

Whitaker, J. S., and C. A. Davis, 1994: Cyclogenesis in a saturated environment. *J. Atmos. Sci.,* **51,** 889–907.